







Hall mobilities and sheet carrier densities in a single LiNbO_3 conductive ferroelectric domain wall

Henrik Beccard ¹, Elke Beyreuther ^{1,*}, Benjamin Kirbus ¹,
Samuel D. Seddon ¹, Michael Rüsing ^{1,2} and Lukas M. Eng ^{1,3}

¹*Institute of Applied Physics, Technische Universität Dresden, Nöthnitzer Strasse 61, 01187 Dresden, Germany*

²*Integrated Quantum Optics, Institute for Photonic Quantum Systems (PhoQS), Paderborn University, 33098 Paderborn, Germany*

³*ct.qmat: Dresden-Würzburg Cluster of Excellence–EXC 2147,
Technische Universität Dresden, 01062 Dresden, Germany*

(Dated: November 7, 2023)

For the last decade, conductive domain walls (CDWs) in single crystals of the uniaxial model ferroelectric lithium niobate (LiNbO_3 , LNO) have shown to reach resistances more than 10 orders of magnitude lower as compared to the surrounding bulk, with charge carriers being firmly confined to sheets of a few nanometers in width. LNO thus currently witnesses an increased attention since bearing the potential for variably designing room-temperature nanoelectronic circuits and devices based on such CDWs. In this context, the reliable determination of the fundamental transport parameters of LNO CDWs, in particular the 2D charge carrier density n_{2D} and the Hall mobility μ_H of the majority carriers, are of highest interest. In this contribution, we present and apply a robust and easy-to-prepare Hall-effect measurement setup by adapting the standard 4-probe van-der-Pauw method to contact a single, hexagonally-shaped domain wall that fully penetrates the 200- μm -thick LNO bulk single crystal. We then determine n_{2D} and μ_H for a set of external magnetic fields B and prove the expected cosine-like angular dependence of the Hall voltage. Lastly, we present photo-Hall measurements of one and the same DW, by determining the impact of super-bandgap illumination on the 2D charge carrier density n_{2D} .

Keywords: ferroelectrics, domain walls, domain wall conductivity, Hall effect, photo-Hall effect, single crystals, lithium niobate, LiNbO_3 , van-der-Pauw, confinement, 2D charge carrier density, 2D electron gas, 2DEG.

I. INTRODUCTION

Continuous progress in solid-state nanotechnology relies on answering a number of unsolved scientific questions with respect to both material systems and device operation principles. One such burning issue is electrical transport under well-defined and controlled conditions in reduced dimensions, as are the 2-dimensional (2D) material systems. While, for example, the 2D van-der-Waals materials are thoroughly analyzed [1], our focus here lies on 2D sheets built up from conductive ferroelectric domain walls (CDWs), i.e., the transition regions between ferroelectric domains of opposite dielectric polarization, which can be tuned to exhibit a strongly enhanced conductivity as compared to the surrounding bulk [2, 3]. In fact, DWs in ferroelectrics have been reported to form effective 2D electron gases (2DEGs) after applying specialized preparation routines to these wide-bandgap bulk materials [4, 5]. LiNbO_3 (LNO) turned out to be *the* “drosophila” ferroelectric for CDW engineering, since it is robust, semiconductor compatible, and easy-to-reconfigure at room temperature, while being commercially available both as a bulk material and in crystalline thin-film-on-insulator form [6–9]. Notably, this ever rising interest in CDWs has been reviewed with respect to both theoretical and device oriented aspects in a number of excellent works [10–17].

At the fundamental level, primarily, the divergence of the ferroelectric polarization (i.e., the local vector field that describes the volume density of unit cell dipoles) at the DW has been identified as one of the main driving forces behind the localized DW conductivity, that, not to forget, has been pre-

dicted already in the 1970s [18]. This divergence is understood as an intrinsic charge density acting as the source of the so-called depolarization field. In turn, the emergent electrostatic field leads to the attraction of free charge carriers to the DWs, as well as to the population of otherwise free electron and/or hole states due to local band bending at the DW position. For the simplest case of a uniaxial ferroelectric (as is LNO) that shows purely Ising-type DWs, this divergence is directly related to the geometrical inclination of the DW with respect to the polar axis [2, 19].

Nevertheless, on a practical level, the determination of DW-related quantitative transport data such as the charge carrier type, density, and mobility, was, to date, restricted to a few exemplary cases, only. In this context, especially the analysis of the Hall effect in DWs in the improper ferroelectrics YbMnO_3 and ErMnO_3 has shown to be a valuable tool, as reported in the groundbreaking papers of Campbell *et al.* [20] and Turner *et al.* [21], respectively. Those authors chose scanning-probe-based approaches for their evaluation, needing a cumbersome and sophisticated procedure to disentangle the Hall potential from the cantilever-based three-terminal reading via calibration routines and accompanying simulations. Moreover, as these authors state themselves, their approach is mainly valid to extract near-surface charge carrier densities and mobilities, only. With respect to proper ferroelectrics, the Hall-effect investigation by Qian *et al.* [22] of DW pn-junctions engineered into x-cut thin-film lithium niobate (TFLN), was equally limited to surface-near carrier densities, while McCluskey *et al.* [23] made use of the fact that a DW in z-cut TFLN mirrors the Corbino cone geometry and in turn found promisingly high carrier mobilities, which were extracted from a magnetoresistance analysis. Notably, the recent study by Beccard *et al.* [5] proposes a completely different approach, quantifying both the 2D charge carrier den-

* elke.beyreuther@tu-dresden.de

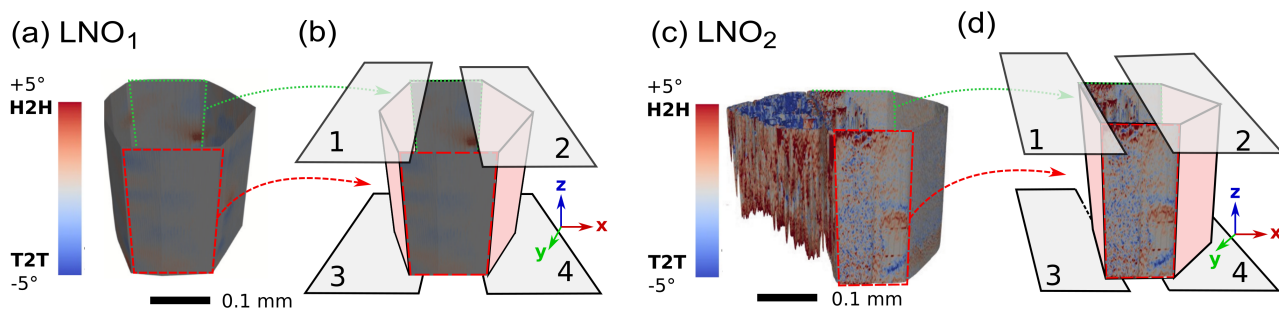


FIG. 1. (a,c) 3D Cherenkov second-harmonic generation microscopy (CSHG) data, and (b,d) chromium electrode arrangement 1–4 for the two samples "LNO₁" and "LNO₂", as prepared from z-cut LiNbO₃ single crystals for Hall-transport measurements using the van-der-Pauw method. Note that contacts 1–4 include a parallel junction of 2 conductive domain walls (CDWs), one in the front (red, dashed) and one in the back (green, dotted). The different protocols applied for domain-wall conductivity (DWC) enhancement in "LNO₁" (a,b) and "LNO₂" (c,d) resulted in the different shape and appearance, as seen in (a,c). The enhanced and desired head-to-head ("H2H") DW inclination is color coded in red in the CSHG scale bar, while tail-to-tail type DWs ("T2T") appear in blue. As seen, sample "LNO₂" shows a larger DW inclination enhancement, justifying the larger DW current as compared to sample LNO₁.

ties n_{2D} and Hall mobilities μ_H through "macroscopic" Hall-effect measurements, by adapting the classical van-der-Pauw (vdP) [24] four-point electrode configuration to measurements from a single CDW in bulk BaTiO₃.

The work presented in this paper sets in exactly at this point, by adopting the vdP scenario to the particular case of a single CDW in z-cut bulk LiNbO₃, the uniaxial model ferroelectric of uttermost importance for prospective nanoscale applications. While significantly high DW conductivity (DWC) in LNO has been proven for the last decade in a number of consecutive works [2, 3, 25, 26], Hall-effect measurements in LNO CDWs are still lacking. In fact, the challenge consists in adapting the vdP method to the hexagonally-shaped DW in LNO as depicted in Fig. 1; as seen, the four vdP contacts then likely measure the parallel junction of two such conductive DWs in LNO, rather than connecting to one single planar 2D sheet as was the case for the CDW in BaTiO₃ [5]. Nonetheless, in the following we will show that evaluating the DW sheet resistance and the magnetic-field dependent Hall voltages still allows applying the vdP method, hence revealing quantitative data for both n_{2D} and μ_H on a so far unprecedented level and precision. In fact, the error stemming from the parallel DW junction is a factor of two in maximum, as easily figured when calculating the total resistance of a parallel junction of two identical / different resistors, i.e., two CDWs. Notably, this factor of two does not change the order of magnitude of both n_{2D} and μ_H . In addition, the same error factor of two is obtained when analyzing the Hall-data in a more rigorous way by applying the concept of the resistor network (RN) [27], as is discussed in the SI-section D.

Moreover, the integrity of the results obtained by the vdP method is corroborated here by two further investigations, (i) by quantifying the angular Hall-voltage dependence, and (ii) when inspecting the Hall-voltage response under super-bandgap illumination for purposely generating additional electron-hole pairs within the CDW.

II. MATERIALS AND METHODS

A. Samples – Fabrication of Domain Walls

For our study here, we employed two 5-mol% Mg-doped congruent z-cut LiNbO₃ crystal plates, with sizes of approx. $1 \times 0.5 \text{ mm}^2$ in the xy-plane and a thickness of 200 μm in the polar z-direction, cut from a commercial wafer by Yamaju Ceramics Co., Ltd.. In the following, we label these samples as "LNO₁" and "LNO₂". A single, fully penetrating and hexagonally-shaped ferroelectric domain of a 257 μm (LNO₁) and 356 μm (LNO₂) diameter [SI-Figs. S7(a) and (b)] was then grown into these samples by applying the well-established method of UV-assisted poling [25, 28] using liquid electrodes and a He-Cd laser (Kimmon Koha IK3301R-G) operated at a 325 nm wavelength, for more details refer, e.g., to [25, 29]. Then, four 8-nm-thick chromium electrodes were vapor-deposited under high-vacuum conditions onto every DW structure, using a shadow mask. The exact electrode geometry and arrangement with respect to the two crystals and DW orientations are sketched in Fig. 1(b,d), while a polarization-sensitive microscopy top-view image is found in the SI-Fig. S7(c). In the following, the electrodes are consecutively labelled by indices 1–4, as standard to 4-point van-der-Pauw experiments. As a result, the 4 vdP electrodes 1–4 directly contact to the two DWs that lie in the xz-plane, one in the front (red, dashed), one in the back (green, dotted), as seen in Fig. 1 for samples "LNO₁" and "LNO₂", respectively. Note that in parallel, two monodomain reference samples "LNO₃" and "LNO₄" were prepared as well, having identical electrodes 1 – 4, but containing no DWs.

B. Enhancement of the Domain Wall Conductivity

Subsequently, the as-grown hexagonal DWs in samples "LNO₁" and "LNO₂" underwent the DWC "enhancement"

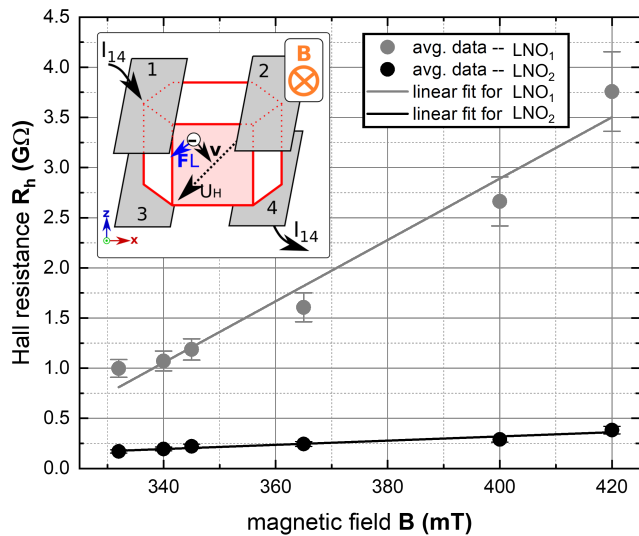


FIG. 2. Results of the macroscopic Hall-effect measurements for samples LNO₁ and LNO₂, carried out as sketched by the inset. The B -field was applied perpendicular to the CDWs and then swept both positively and negatively. The charge carriers, i.e., mainly electrons – as discussed in the text – that flow between the current contacts 1 and 4 are deflected by the Lorentz force F_L resulting in a measurable Hall voltage $U_H = U_{23}$ read between contacts 2 and 3. Plotted in the main diagram is the Hall resistance $R_h = U_{23}/I_{14}$ as a function of B -field for the two samples, with sample LNO₂ showing a nearly 10-times larger response. Note that the plotted R_h values are the averaged values of $R_h(+B)$ and $R_h(-B)$ in order to compensate for sample misalignment effects [see raw data in SI-Fig. S5, and the reference U_H measurement recorded from a monodomain bulk LNO crystal (containing no CDW at all) in SI-Fig. S6(a)]. The corresponding 2D charge carrier densities n_{2D} were then extracted from the slope of these linear relationships according to eq. (1) and are discussed further down as well as summarized in Tab. I.

procedure by applying high voltages between the $z+$ and $z-$ sides supplied by the voltage source of a Keithley 6517B electrometer, as described previously in refs. [2, 3]. The corresponding current-voltage curves recorded during these voltage ramps are depicted in SI-Fig. S1, and the exact parameters of the post-growth treatment are stated in the SI-tab. S1. Our enhancement procedure leads to higher average DW inclination angles relative to the polar z -axis and, in turn, to stronger DW confined charge accumulation and thus to a larger DW conductivity. However, in order to possibly break up the initial parallel DW junction arrangement [see again Fig. 1] and to apply our Hall-effect measurements to a single CDW, the enhancement procedure here was realized differently and deliberately asymmetrical for the two LNO samples. In particular, we treated sample LNO₁ with only one high-voltage ramp between electrodes 1 and 3, while sample LNO₂ experienced consecutive voltage ramps between both top-bottom electrode pairs 1/3 and 2/4, respectively, cf. SI-tab. S1 and SI-Fig. S1. Accompanying images by 3D Cherenkov second-harmonic generation microscopy (CSHG), our standard non-destructive and real-space method of choice for both visualizing ferroelectric DWs [3, 30, 31] and especially for correlating their

local inclination to the DW conductivity, indeed elucidates a very different DW appearance for samples LNO₁ and LNO₂ [see Fig. 1(a) and (c)] with average inclination angles between 0° and 0.5° and broad inclination distributions. The two different enhancement procedures for samples LNO₁ and LNO₂ are clearly reflected in the two CSHG pictures in Fig. 1(a),(c), where the walls in LNO₂ show on average a much larger distribution of angles suggesting a larger local screening charge, which is later reflected in the carrier densities; nonetheless, the overall DW conductivities could be readily enhanced for both cases, by three (LNO₁) and six (LNO₂) orders of magnitude in maximum (cf. SI-Fig. S2(a) and (b) and SI-tab. S1). The detailed current-voltage characteristics recorded between the different electrode pairs can be found in the Supplemental Information, part A.

C. Realization of Hall Voltage Measurements

For quantifying the LNO DW Hall voltage, the adapted vdP configuration [24] was employed as illustrated in the inset of Fig. 2 and, within a previous study, successfully tested for 2DEGs in BaTiO₃ CDWs [5]. The sample therefore was mounted into an electromagnet at room temperature that delivers magnetic fields B of up to ± 420 mT. Contacts 1 and 4 were connected to the Keithley 6517B electrometer to apply a bias voltage of 6 V, which resulted in a domain wall current $I = I_{14}$ on the order of 0.1 nA. The corresponding carriers hence experience the Lorentz force F_L as sketched in the inset of Fig. 2, resulting in the Hall voltage $U_H := U_{23}$ that is detected between contacts 2 and 3 using a Keithley 2700 multimeter. The ratio $R_h = U_H/I$, subsequently denoted as the Hall resistance, was determined for six different B -field values set between 330 mT and 420 mT. In order to account for any sample misalignment within the electromagnet (i.e. non-parallel alignment of B -field and DW normal vector), the B -field direction was switched by changing the sign of the electromagnet's voltage, and the measurement series was repeated – a common practice for Hall voltage measurements[32]. The corresponding data set was acquired for both DW samples LNO₁ and LNO₂ (see Fig. 2 for the averaged data and SI-Fig. S5 for the raw data, i.e., the B -field-direction dependent data).

D. Angular Dependence of the Hall Voltage

Now, to verify that a true Hall voltage and not a parasitic quantity is measured, the angular dependence $U_H(\Phi)$ was recorded next, by mounting sample LNO₂ on a rotation table inside the electromagnet. Here, Φ denotes the angle between magnetic field vector B and the plane of carrier transport, varying between 0° and 90° in a cosine fashion [see inset of Fig. 3(a)]. $U_H(\Phi)$ was then recorded for a fixed B -field of 400 mT at 5 different Φ values including 0° and 90° . The data is plotted in Fig. 3(a), and clearly shows the expected Hall-voltage behavior, especially also recording $U_H(\Phi = 90^\circ) = 0$.

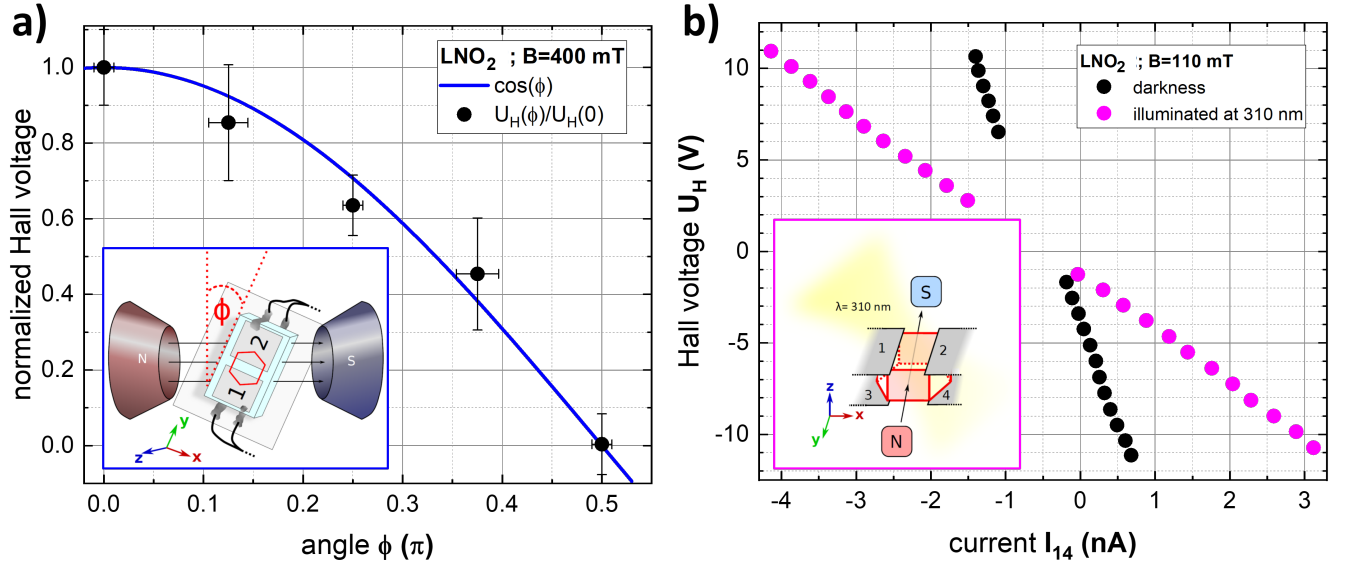


FIG. 3. (a) The DW of sample LNO₂ was exemplarily rotated in the B -field of the electromagnet, with the angle Φ being varied between 0 and 90° and the corresponding Hall voltages measured, as sketched in the inset. As expected, the Hall voltage U_H decreases when changing Φ from 0° to 90° and the ratio $U_H/U_{H,0}$ with $U_{H,0}$ being the Hall voltage at 0° (i.e., with the magnetic field vector being aligned perpendicular to both the CDW and the injected current) follows the theoretically predicted cosine function very clearly. All data points were acquired with a constant magnetic field of 400 mT. (b) Impact of super-bandgap illumination on the Hall transport for sample LNO₂, which was placed in a constant field of $B = 110$ mT supplied by a permanent magnet and illuminated at a wavelength of 310 nm under a constant photon flux of 10^{13} s^{-1} . The Hall voltage $U_H = U_{23}$ was recorded as a function of the current $I = I_{14}$ for the two cases: (i) under illumination (purple data points) and (ii) in the dark (black data points). Both data sets show a linear behavior, however, with a significantly increased response when illuminating the DW, then generating additional electron-hole pairs.

E. Hall Voltage under Super-Bandgap Illumination

A second independent integrity experiment, carried out also only with specimen LNO₂, investigated the influence of super-bandgap illumination on the DW current, which is expected to significantly enlarge the sheet carrier density n_{2D} by generating electron-hole pairs that then must decrease R_h and U_H . For this complementary test the DW of LNO₂ was placed in a 110-mT field of a permanent magnet with $\Phi = 0^\circ$, and then illuminated at a 310 nm wavelength, which corresponds to the optical band gap of $E_g = 4.0$ eV for bulk 5-mol% Mg-doped LiNbO₃ [25]. A 1000-W Xe arc lamp coupled into a grating monochromator (Cornerstone 260 by Oriel Instruments) and focused onto the whole $5 \times 10 \text{ mm}^2$ sample area served as the photo-exciting light source applying a constant photon flux of 10^{13} s^{-1} [see sketch in Fig. 3(b)]. Using this setup, U_H was then acquired as a function of DW-current I both with/without light. The data are displayed in Fig. 3(b).

F. Theoretical Background for the Extraction of Sheet Carrier Densities and Hall Mobilities

Prior to discussing the results of these experiments, we briefly summarize here the mathematical background that is needed to extract both the charge carrier densities n_{2D} and the Hall mobilities μ_H from our experimental data. The full discussion was explained step-by-step in Beccard *et al.* [5],

where we had already underlined the indispensable necessity for offset and error corrections in vdP experiments as outlined by Werner [32]. To interpret our Hall data, we assume (A) that the DW current is established by electrons as the majority charge carriers. That the majority carrier are negative was derived from a preliminary experiment testing simply the polarity of the Hall voltage. The assumption that these carriers are very probably electrons is derived from two recent studies: first, via in-situ strain experiments for a set of equivalently prepared DWs based on crystal pieces of LNO wafers from the same manufacturer [33] and which can be understood due to their superior mobility compared to holes and the positive bound charges at a head-to-head (H2H)-DW requiring negative screening charges [26, 34]; and second, via temperature-dependent DWC measurements revealing activation energies in the range of 100-250 meV [35] and thus pointing towards electron-polaron mediated hopping with ionic transport being very improbable. And (B), we assume that the magnetic field stands perpendicular to the conductive layer, i.e., the CDW. Then, the Hall voltage U_H follows [36, 37] the relationship $U_H = \frac{I \cdot B}{q \cdot n \cdot d}$ with B the absolute value of the magnetic field, I the current driven through the conducting DW layer (in particular: $I = I_{14}$), q the elementary charge, d the DW width, and n the 3D charge carrier density. Introducing the 2D charge carrier density n_{2D} , also referred to as sheet carrier density, with $n_{2D} = n \cdot d$ and the Hall resistance $R_h = U_H/I = U_{23}/I_{14}$, the former can be extracted from the slope of the (measured) expected linear R_h -vs.- B dependence as:

$$R_h \propto \frac{B}{q \cdot n_{2D}} \quad (1)$$

For the subsequent calculation of the Hall mobility μ_H of the majority charge carriers, we employ the relation:

$$\mu_H = \frac{1}{q \cdot n_{2D} \cdot R_S} \quad (2)$$

Note that the Hall mobility μ_H is linked to the "actual" mobility μ via the Hall factor R_h as $\mu_H = R_h \cdot \mu$. The Hall factor, which depends on internal scattering mechanisms, is not known in most practical cases and commonly assumed to be unity [20]. Furthermore, R_S is the sheet resistance of the CDW, which is readily obtained by solving van der Pauw's equation numerically [37]:

$$\exp\left(-\frac{\pi}{R_S} R_{13,42}\right) + \exp\left(-\frac{\pi}{R_S} R_{34,21}\right) = 1 \quad (3)$$

$R_{13,42} = U_{42}/I_{13}$ and $R_{34,21} = U_{21}/I_{34}$ are easily extracted from corresponding current injection and voltage measurements between the respective contacts. The values measured here are all listed in SI-table S3.

III. RESULTS AND DISCUSSION

As key findings of our study, the measured relationship between $R_h = U_H/I$ and the absolute value of the magnetic field B normal to the DW is depicted for both DWs in Fig. 2. The corresponding raw data before averaging over both field directions can be found in the SI-Fig. S5, while an additional averaging over the two possible current directions as in refs. [5, 32] could not be realized due to the rectifying character of the U_{23} -vs- I_{14} curves. According to eq. (1), rewritten as $R_h \propto b \cdot B$ with the slope $b = \frac{1}{q \cdot n_{2D}}$, very clear and linear dependencies of the Hall resistance R_h vs. magnetic field B curves are indeed observed experimentally here for the DWs in both LNO samples. The corresponding slopes were extracted from the linear fits. They read as $b_1 = (31 \pm 3) \cdot 10^9 \Omega T^{-1}$ as well as $b_2 = (21 \pm 3) \cdot 10^8 \Omega T^{-1}$ for samples LNO₁ and LNO₂, respectively. Table I summarizes the sheet carrier densities n_{2D} as extracted from these slopes. The numerical values for n_{2D} cover two orders of magnitude for the two specimen, with LNO₂ showing the larger n_{2D} value of $3 \times 10^5 \text{ cm}^{-2}$, which is two orders of magnitude more than recently observed in conductive BaTiO₃ DWs, and moreover, a very reasonable value for a 2D electronic system [5]. Reconsidering the findings of the CSHG imaging [cf. Fig. 1(a),(c)] the n_{2D} -discrepancy between LNO₁ and LNO₂ is not a surprise, since the DW of LNO₂ shows a broader range of DW inclination angles. Consequently, a higher charge carrier reservoir in contrast to LNO₁ is obviously expected. In other words, the link between DW geometry, or more generally, the DW's real structure, and

electrical performance, is reflected in the present Hall-effect results.

In principle, the 3D charge carrier density $n = n_{2D}/d$ can be calculated as well, provided the DW width d is known. Nevertheless, for the two specimen here d is unknown, but to tentatively estimate typical values we use the literature value of 174 pm, which was derived from transmission electron microscopy (TEM) by Gonnissen *et al.* [38] on macroscopically non-inclined LNO domain walls, and receive carrier densities n reading $1.15 \cdot 10^{12} \text{ cm}^{-3}$ for LNO₁ and $17 \cdot 10^{12} \text{ cm}^{-3}$ for LNO₂, respectively. However, as of now it is not clear, (i) whether the width of our conductivity-enhanced DWs here is comparable with the width of the DWs as measured by Gonnissen *et al.*, and (ii) to what extent the transport channel is different in width compared to the width defined by the polarization change as measured via TEM, i.e., whether screening charges are trapped in a larger area. Therefore, the above values for n should be seen as first "qualified guesses".

TABLE I. Overview of the DW parameters, i.e., the sheet resistance R_S (for their graphical determination see SI-tab. S3 and SI-fig. S4), the 2-dimensional charge carrier density n_{2D} , and the Hall mobility μ_H , as extracted from DW-confined Hall effect measurements using eqs. (1)–(3).

sample	R_S ($10^{12} \Omega/\square$)	n_{2D} ($10^3/\text{cm}^2$)	μ_H (cm^2/Vs)
LNO ₁	5.6	20 ± 2	54 ± 5
LNO ₂	0.6	297 ± 36	35 ± 4

The second quantity evaluated from our four-point probe setup employing eqs. (2) and (3), is the Hall mobility μ_H . The extracted values are listed in Tab. I as well. In comparison to mobilities of LNO *bulk* that have been reported [39] to be $0.8 \text{ cm}^2/\text{Vs}$, the *domain walls'* Hall mobilities found here are significantly (almost 2 orders of magnitude) higher, which is an expected and desirable result. On the other hand, the Hall mobilities in *thin-film based* LNO domain walls, which were reported by Qian *et al.* [22] ($337.30 \text{ cm}^2/\text{Vs}$) and McCluskey *et al.* [23] (around $3700 \text{ cm}^2/\text{Vs}$) are 1–2 orders of magnitude larger once more and it will be a future experimental challenge to investigate whether these ranges can be achieved within LNO single crystal DWs as well. One may question to what extent the preconditions that justify eq. (3), are satisfied for the DWs of the current study. In an ideal case, the conducting sheet in the van-der-Pauw configuration has to be homogeneous, isotropic, uniform in thickness, without holes, and the contacts have to be point contacts at the perimeter. Reconsidering the CSHG-microscopy images showing a significant range of inclination angles and a tendency towards spike domain formation at least for sample LNO₂ and the fact that the LNO DWs are more tube-like rather than forming a 2D sheet, it appears to be necessary to estimate these errors as induced by these non-idealities:

In the simplest case and as indicated in Fig. 1(b,d), the Hall transport in samples LNO₁ and LNO₂ can be assumed as a parallel conduction through two identical DW sheets, which

would mean a factor of 2 between the measured current and the current flowing through one of the two sheets, i.e., in turn, n_{2D} would be diminished by a factor of 2. Accounting for the more complex real structure of the CDWs in samples LNO₁ and LNO₂ [see Fig. 1(a,c)] we accomplished resistor-network simulations as described in detail earlier [27] and briefly explicated in SI-section D, with the rather similar result that the determined charge carrier densities are on the same order of magnitude needing correction factors of 0.51 and 0.65 for sample LNO₁ and LNO₂, respectively (see SI-sec. D). Note that the other extreme case, i.e., a strongly asymmetric conductivity of the two parallel DW sheets, would not need such a correction, since the measurement would reflect mainly the "Hall-behavior" of the highly conductive DW. Against the background that in a Hall scenario primarily the *order of magnitude* of carrier densities and mobilities are of interest, correction factors between 0.5 and 1 are fully acceptable in any case.

Nevertheless, the non-ideal fitting to the van-der-Pauw restrictions gave further motivation to test the integrity of the approach by additional Hall-effect measurements:

In a first supporting experiment we recorded the dependence of U_H on the angle Φ enclosed between magnetic field B and conducting sheet as exemplarily illustrated in Fig. 3(a) for sample LNO₂, i.e., the DW with the largest charge carrier density and the lowest sheet resistance. As seen from the plot of the normalized Hall voltage $U_H/U_{H,0}$ versus angle Φ , the expected cosine behavior is convincingly reproduced by the measured data.

In a second additional experiment illustrated in Fig. 3(b) performed again with the DW of specimen LNO₂, we studied whether super-bandgap illumination at 310 nm, which corresponds to the optical bandgap of Mg-doped LiNbO₃ of 4.0 eV, might impact the Hall voltage. In fact, the earliest experiments focusing on measuring the DW conductivity in LNO had already qualitatively reported that super-bandgap light strongly enhances the charge carrier density at DWs [25]. Indeed, the slope of the U_H -vs.- I decreases under UV illumination, as shown in Fig. 3(b), indicating a decrease in R_h and hence an increase in the sheet carrier density n_{2D} , as follows from eq. (1). The numerical evaluation of the slope via linear curve fitting yields a significant increase of the carrier density by a factor of 4–5 under super-bandgap excitation with a rather moderate photon flux. In the control experiment where a monodomain z-cut LiNbO₃ bulk crystal (i.e., without hexagonal domain structures) was covered with the same electrode configuration and tested in the same type of measurement scenario, a bulk photo-Hall effect could be excluded, since no functional relationship between the driving current I_{14} and the Hall voltage U_{23} apart from noise was observed [SI-Fig. S6(b)]. Thus, we state that the proposed Hall-effect measurement setup is also efficient for investigating the photo-induced DW-confined transport behavior, which clearly opens up the box to implement DW-based devices for nano-optoelectronic applications as well.

IV. CONCLUSION

In summary, two exemplary conductive ferroelectric domain walls, engineered into a z-cut 200- μm -thick 5-mol% MgO-doped LiNbO₃ single crystal, completely penetrating the latter, and shaped like hexagonal tubes with, however, different microscopic real structure, were macroscopically electrically connected with four Cr electrodes (two on the z^+ and two on the z^- surface) in order to set up a van-der-Pauw four-point-probe geometry for Hall probing. This setting in turn was employed for measuring the Hall resistance R_h as a function of the magnetic field B applied perpendicular to two of the six side sheets of the hexagonally-shaped DW tubes, as well as the sheet resistance R_s of the DWs, which finally allowed us to extract two characteristic key quantities for such low-dimensional electronic systems, i.e., the 2D charge carrier density n_{2D} found to be in the range $20\text{...}300\cdot 10^{12}\text{cm}^{-2}$ and the Hall mobility μ_H (extracted as 54 and 35 $\text{cm}^2(\text{Vs})^{-1}$ for the two samples, respectively, with a reasonable error around 10%). The validity of these numbers was further tested through angle- and illumination dependent Hall-voltage recordings, which both showed the expected behavior. Moreover, we employed resistor-network simulations to calculate correction factors for n_{2D} and μ_h , due to the parallel junction formed by the two CDWs, which were in the range of 0.5 and thus did not change the order of magnitude of the two quantities. Thus we propose that macroscopic Hall-effect analysis, as applied here, provides a robust and versatile method for the comparative quantification of the electrical performance of conductive domain walls in both LNO and many other materials. Moreover, photo-induced Hall measurements might gain even more interest, especially also for realizing nano-optoelectronic circuits.

ACKNOWLEDGEMENTS

We acknowledge financial support by the Deutsche Forschungsgemeinschaft (DFG) through joint DFG–ANR project TOPELEC (EN 434/41-1 and ANR-18-CE92-0052-1), the CRC 1415 (ID: 417590517) the FOR 5044 (ID: 426703838; <https://www.for5044.de>) as well as through the Würzburg-Dresden Cluster of Excellence on "Complexity and Topology in Quantum Matter" - ct.qmat (EXC 2147, ID: 39085490). This work was supported by the Light Microscopy Facility, a Core Facility of the CMCB Technology Platform at TU Dresden.

DATA AVAILABILITY

The data that support the findings of this study are available from the corresponding author upon reasonable request.

- [1] K. S. Novoselov, A. Mishchenko, A. Carvalho, and A. H. C. Neto, 2D materials and van der Waals heterostructures, *Science* **353**, aac9439 (2016).
- [2] C. Godau, T. Kämpfe, A. Thiessen, L. Eng, and A. Haußmann, Enhancing the domain wall conductivity in lithium niobate single crystals, *ACS Nano* **11**, 4816 (2017).
- [3] B. Kirbus, C. Godau, L. Wehmeier, H. Beccard, E. Beyreuther, A. Haußmann, and L. Eng, Real-time 3d imaging of nanoscale ferroelectric domain wall dynamics in lithium niobate single crystals under electric stimuli: Implications for domain-wall-based nanoelectronic devices, *ACS Applied Nano Materials* **2**, 5787 (2019).
- [4] T. Sluka, A. Tagantsev, P. Bednyakov, and N. Setter, Free-electron gas at charged domain walls in insulating BaTiO₃, *Nature Communications* **4**, 1808 (2013).
- [5] H. Beccard, B. Kirbus, E. Beyreuther, M. Rüsing, P. Bednyakov, J. Hlinka, and L. M. Eng, Nanoscale Conductive Sheets in Ferroelectric BaTiO₃: Large Hall Electron Mobilities at Head-to-Head Domain Walls, *ACS Applied Nano Materials* **5**, 8717 (2022).
- [6] M. Rusing, P. O. Weigel, J. Zhao, and S. Mookherjea, Toward 3D Integrated Photonics Including Lithium Niobate Thin Films: A Bridge Between Electronics, Radio Frequency, and Optical Technology, *IEEE Nanotechnology Magazine* **13**, 18 (2019).
- [7] D. Zhu, L. Shao, M. Yu, R. Cheng, B. Desiatov, C. J. Xin, Y. Hu, J. Holzgrafe, S. Ghosh, A. Shams-Ansari, E. Puma, N. Sinclair, C. Reimer, M. Zhang, and M. Lončar, Integrated photonics on thin-film lithium niobate, *Advances in Optics and Photonics* **13**, 242 (2021).
- [8] D. Sun, Y. Zhang, D. Wang, W. Song, X. Liu, J. Pang, D. Geng, Y. Sang, and H. Liu, Microstructure and domain engineering of lithium niobate crystal films for integrated photonic applications, *Light: Science & Applications* **9**, 197 (2020).
- [9] T. Kämpfe, B. Wang, A. Haußmann, L.-Q. Chen, and L. M. Eng, Tunable Non-Volatile Memory by Conductive Ferroelectric Domain Walls in Lithium Niobate Thin Films, *Crystals* **10**, 804 (2020).
- [10] G. Catalan, J. Seidel, R. Ramesh, and J. F. Scott, Domain wall nanoelectronics, *Review of Modern Physics* **84**, 119 (2012).
- [11] D. Meier, Functional domain walls in multiferroics, *Journal of Physics: Condensed Matter* **27**, 463003 (2015).
- [12] T. Sluka, P. Bednyakov, P. Yudin, A. Crassous, and A. Tagantsev, Charged domain walls in ferroelectrics, in *Topological Structures in Ferroic Materials: Domain Walls, Vortices and Skyrmions*, edited by J. Seidel (Springer International Publishing, Cham, 2016) pp. 103–138.
- [13] P. S. Bednyakov, B. I. Sturman, T. Sluka, A. K. Tagantsev, and P. V. Yudin, Physics and applications of charged domain walls, *npj Computational Materials* **4**, 65 (2018).
- [14] P. Sharma, P. Schoenherr, and J. Seidel, Functional ferroic domain walls for nanoelectronics, *Materials* **12**, 2927 (2019).
- [15] G. Nataf, M. Guennou, J. Gregg, D. Meier, J. Hlinka, E. K. H. Salje, and J. Kreisel, Domain-wall engineering and topological defects in ferroelectric and ferroelastic materials, *Nature Reviews Physics* **2**, 634 (2020).
- [16] D. Meier and S. Selbach, Ferroelectric domain walls for nanotechnology, *Nature Reviews Materials* **7**, 157 (2021).
- [17] P. Sharma, T. S. Moise, L. Colombo, and J. Seidel, Roadmap for ferroelectric domain wall nanoelectronics, *Advanced Functional Materials* **32**, 2110263 (2022).
- [18] B. M. Vul, G. M. Guro, and I. I. Ivanchik, Encountering domains in ferroelectrics, *Ferroelectrics* **6**, 29 (1973).
- [19] E. Eliseev, A. Morozovska, G. Svecnikov, V. Gopalan, and V. Y. Shur, Static conductivity of charged domain walls in uniaxial ferroelectric semiconductors, *Physical Review B* **83**, 235313 (2011).
- [20] M. Campbell, J. McConville, R. McQuaid, D. Prabhakaran, A. Kumar, and J. Gregg, Hall effect in charged conducting ferroelectric domain walls, *Nature Communications* **7**, 13764 (2016).
- [21] P. Turner, J. McConville, S. McCartan, M. Campbell, J. Schaab, R. McQuaid, A. Kumar, and J. Gregg, Large carrier mobilities in ErMnO₃ conducting domain walls revealed by quantitative Hall-effect measurements, *Nano Letters* **18**, 6381 (2018).
- [22] Y. Qian, Y. Zhang, J. Xu, and G. Zhang, Domain-Wall p - n Junction in Lithium Niobate Thin Film on an Insulator, *Physical Review Applied* **17**, 044011 (2022).
- [23] C. J. McCluskey, M. G. Colbear, J. P. V. McConville, S. J. McCartan, J. R. Maguire, M. Conroy, K. Moore, A. Harvey, F. Trier, U. Bangert, A. Gruverman, M. Bibes, A. Kumar, R. G. P. McQuaid, and J. M. Gregg, Ultrahigh Carrier Mobilities in Ferroelectric Domain Wall Corbino Cones at Room Temperature, *Advanced Materials* **34**, 2204298 (2022).
- [24] L. van der Pauw, A method of measuring the resistivity and hall coefficient on lamellae and arbitrary shape, *Philips Technical Review* **20**, 220 (1958).
- [25] M. Schröder, A. Haußmann, A. Thiessen, E. Soergel, T. Woike, and L. Eng, Conducting domain walls in lithium niobate single crystals, *Advanced Functional Materials* **22**, 3936 (2012).
- [26] C. Werner, S. Herr, K. Buse, B. Sturman, E. Soergel, C. Razzaghi, and I. Breunig, Large and accessible conductivity of charged domain walls in lithium niobate, *Scientific Reports* **7**, 9862 (2017).
- [27] B. Wolba, J. Seidel, C. Cazorla, C. Godau, A. Haußmann, and L. Eng, Resistor Network Modeling of Conductive Domain Walls in Lithium Niobate, *Advanced Electronic Materials* **4**, 1700242 (2018).
- [28] M. Wengler, U. Heinemeyer, E. Soergel, and K. Buse, Ultraviolet light-assisted domain inversion in magnesium-doped lithium niobate crystals, *Journal of Applied Physics* **98**, 064104 (2005).
- [29] I. Kiselva, *Toward Reproducible Domain-Wall Conductance in Lithium Niobate Single Crystals*, Master's thesis, Technische Universität Dresden (2023).
- [30] T. Kämpfe, P. Reichenbach, M. Schröder, A. Haußmann, L. Eng, T. Woike, and E. Soergel, Optical three-dimensional profiling of charged domain walls in ferroelectrics by cherenkov second-harmonic generation, *Physical Review B* **89**, 035314 (2014).
- [31] T. Kämpfe, P. Reichenbach, A. Haußmann, T. Woike, E. Soergel, and L. Eng, Real-time three-dimensional profiling of ferroelectric domain walls, *Applied Physics Letters* **107**, 152905 (2015).
- [32] F. Werner, Hall measurements on low-mobility thin films, *Journal of Applied Physics* **122**, 135306 (2017).
- [33] E. Singh, H. Beccard, Z. H. Amber, J. Ratzenberger, C. W. Hicks, M. Rüsing, and L. M. Eng, Tuning domain wall conductivity in bulk lithium niobate by uniaxial stress, *Physical Review B* **106**, 144103 (2022).
- [34] S. Y. Xiao, T. Kämpfe, Y. M. Jin, A. Haußmann, X. M. Lu, and L. M. Eng, Dipole-Tunneling Model from Asymmetric Domain-Wall Conductivity in LiNbO₃ Single Crystals, *Phys-*

ical Review Applied **10**, 034002 (2018).

- [35] M. Zahn, E. Beyreuther, I. Kiseleva, A. S. Lotfy, C. J. McCluskey, J. R. Maguire, A. Suna, M. Rüsing, J. M. Gregg, and L. M. Eng, R2D2 – An equivalent-circuit model that quantitatively describes domain wall conductivity in ferroelectric LiNbO₃ (2023), arXiv:2307.10322 [cond-mat.mtrl-sci].
- [36] D. K. Schroder, *Semiconductor Material and Device Characterization* (Wiley-VCH, 2006).
- [37] M. Lundstrom, *Fundamentals of carrier transport* (Cambridge University Press, Cambridge, 2000).
- [38] J. Gonnissen, D. Batuk, G. F. Nataf, L. Jones, A. M. Abakumov, S. Van Aert, D. Schryvers, and E. K. H. Salje, Direct Observation of Ferroelectric Domain Walls in LiNbO₃: Wall-Meanders, Kinks, and Local Electric Charges, *Advanced Functional Materials* **26**, 7599 (2016).
- [39] Y. Ohmori, M. Yamaguchi, K. Yoshino, and Y. Inuishi, Electron Hall Mobility in Reduced LiNbO₃, *Japanese Journal of Applied Physics* **15**, 2263 (1976).

SUPPLEMENTARY INFORMATION

A. Compilation of current-voltage (IV) characteristics and derived DW resistances

Here, we assemble a number of current-voltage curves, all of them collected with a Keithley 6517B electrometer, of the two different LNO DWs under investigation in order to complete the overall picture on them.

First of all, the current-voltage characteristics during the high-voltage ramping treatment according to our protocol published earlier [2] (using the voltage source of the Keithley 6517B) is shown in SI-Fig. S1. The corresponding final electrical fields E_{13} and E_{24} (the latter was applied only in case of LNO₂) are listed in SI-tab. S1. The voltage ramp velocity was 10 V per 2 s.

Further, we acquired a number of standard low-voltage current-voltage characteristics between different combinations of electrodes in the range of ± 10 V. Therefore the measuring voltage was swept from -10 V to 10 V using the voltage source of a Keithley 6517B electrometer with waiting intervals of 2 s while subsequently measuring the current by the same device.

SI-Fig. S2 depicts the low-voltage IV-curves in z-direction (polarization direction) between the two electrode pairs. While the enhancement between electrodes 1 and 3 was obviously successful (with "conductivity-enhancement factors" $F_{13}=6\cdot 10^3$ and $5\cdot 10^6$ for LNO₁ and LNO₂, respectively, cf. SI-tab. S1) and led to diode-like characteristics [SI-Fig. S2(a) and (b)], the other side, i.e., the path between electrodes 2 and 4, exhibits ohmic behavior and a detectable but decisively lower conductivity enhancement ($F_{24}=3\cdot 10^3$ and $9\cdot 10^1$) for LNO₁ and LNO₂, respectively. This is not surprising, since for LNO₁ no high-voltage ramp had been driven between this electrode pair intentionally, and in the case of LNO₂ the enhancement protocol was obviously not successful (cf. SI-Fig. S1(b) again).

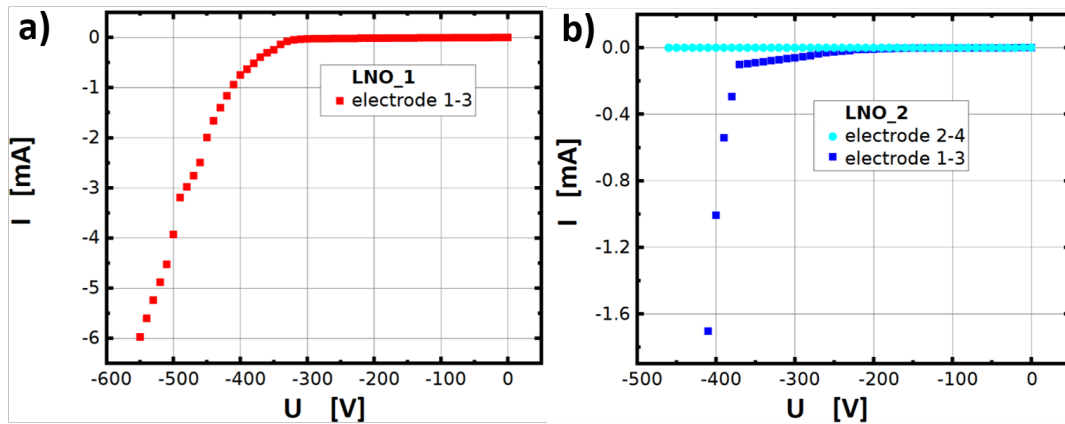


FIG. S1. Current-voltage characteristics logged *during* the high-voltage biasing of the hexagonal LNO domain walls in order to increase the domain wall inclination and thus the DW conductivity according to the protocol of Godau et al. [2]. a) In the case of LNO₁ only one side, i.e., one top-bottom electrode pair (1/3) was used. b) In sample LNO₂ both, the top-bottom pairs 1/3 and 2/4 were treated, whereas only in the first case a significant current flow could be induced. However, as SHG images (cf. Fig. 1(c) of the main text) show, both sides of the hexagonal domain wall showed higher average inclinations with respect to the polar axis than in the case of LNO₁. The resulting after-conductivity-enhancement IV-curves measured in both z-direction and diagonally are shown in the following figures S2 and S3, respectively.

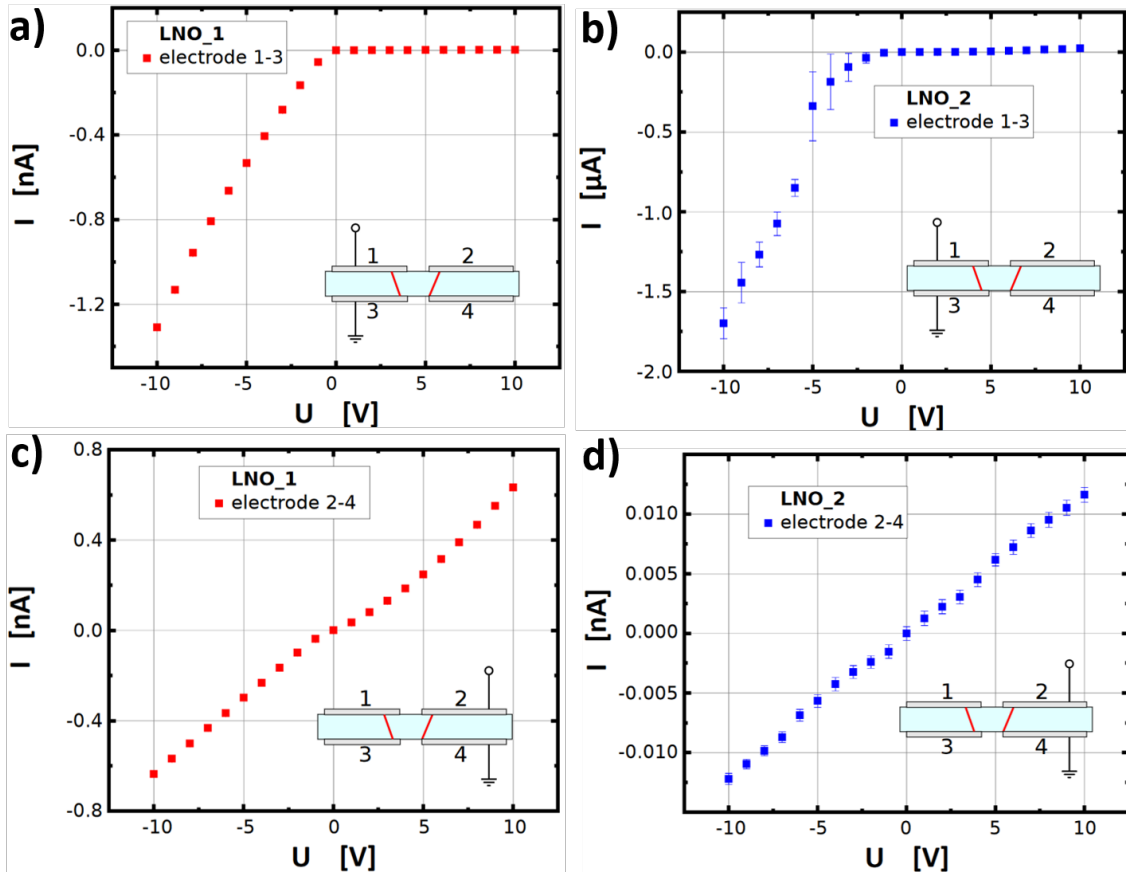


FIG. S2. Current-voltage characteristics in the ± 10 V range as measured along the z -direction between electrodes 1/3 and 2/4, respectively. Panels (a,c) and (b,d) depict the case of LNO₁ and LNO₂, respectively. There is a noticeable similarity between the two samples: The IV-characteristics between electrodes 1/3, which are the electrode pairs having shown a significant "enhancement current" (Fig. S1), are diode like, while the IV-curves for electrodes 2/4 are ohmic-like.

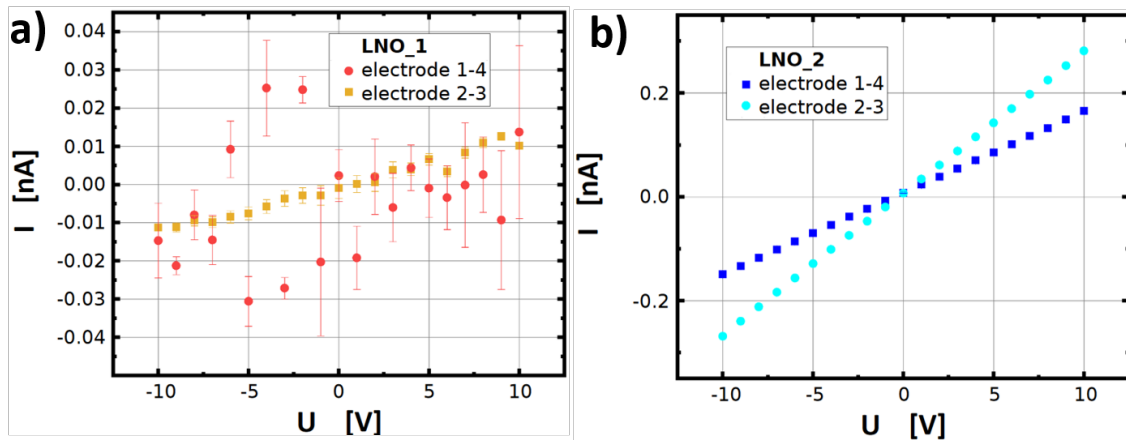


FIG. S3. Post-enhancement diagonal IV-characteristics for the DWs of samples (a) LNO₁ and (b) LNO₂. The corresponding DW resistances, which were extracted from the slopes after linear curve fitting, are listed in tab. S2.

TABLE S1. Overview of selected electrical parameters of the two LNO domain walls of the study: as-grown resistance in z-direction between electrodes 1/3, $R_{13}^{(0)}$; electrical field during the "enhancement" treatment, E_{13} ; post-enhancement resistance in z-direction between electrodes 1/3: in forward direction – $R_{13}^{(forw)}$, in reverse direction – $R_{13}^{(rev)}$; conductivity-enhancement factor $F = R_{13}^{(0)}/R_{13}^{(forw)}$. For the electrode pair 2/4 we use an analogous nomenclature with R_{24} covering the uniform since ohmic "post-enhancement" resistance.

sample	$R_{13}^{(0)}$ (Ω)	E_{13} ($\frac{kV}{mm}$)	$R_{13}^{(forw)}$ (Ω)	F_{13}	$R_{13}^{(rev)}$ (Ω)	$R_{24}^{(0)}$ (Ω)	E_{24} ($\frac{kV}{mm}$)	R_{24} (Ω)	F_{24}
LNO ₁	$71 \cdot 10^{12}$	2.75	$11 \cdot 10^9$	$6 \cdot 10^3$	$0.3 \cdot 10^9$	$57 \cdot 10^{12}$	–	$18 \cdot 10^9$	$3 \cdot 10^3$
LNO ₂	$12 \cdot 10^{12}$	2.05	$2.6 \cdot 10^6$	$5 \cdot 10^6$	$0.4 \cdot 10^9$	$74 \cdot 10^{12}$	2.30	$833 \cdot 10^9$	$9 \cdot 10^1$

TABLE S2. Diagonal resistances R_{14} and R_{23} as measured in the "post-enhancement" state.

sample	R_{14} ($10^9 \Omega$)	R_{23} ($10^9 \Omega$)
LNO ₁	625	847
LNO ₂	50	33

TABLE S3. Measured current and voltage values in van-der-Pauw configuration, as well as following resistance values $R_{13,42}$ and $R_{34,21}$ for the extraction of the sheet resistance R_S (cf. tab. I of the main paper) according to eq. (3) of the main text.

sample	$R_{13,42}$ ($10^{12} \Omega$)	U_{42} (V)	I_{13} (10^{-12} A)	$R_{34,21}$ ($10^{12} \Omega$)	U_{21} (V)	I_{34} (10^{-12} A)
LNO ₁	2	3.7	1.9	0.7	6.2	8.9
LNO ₂	0.18	0.5	2.8	0.1	0.3	2.8

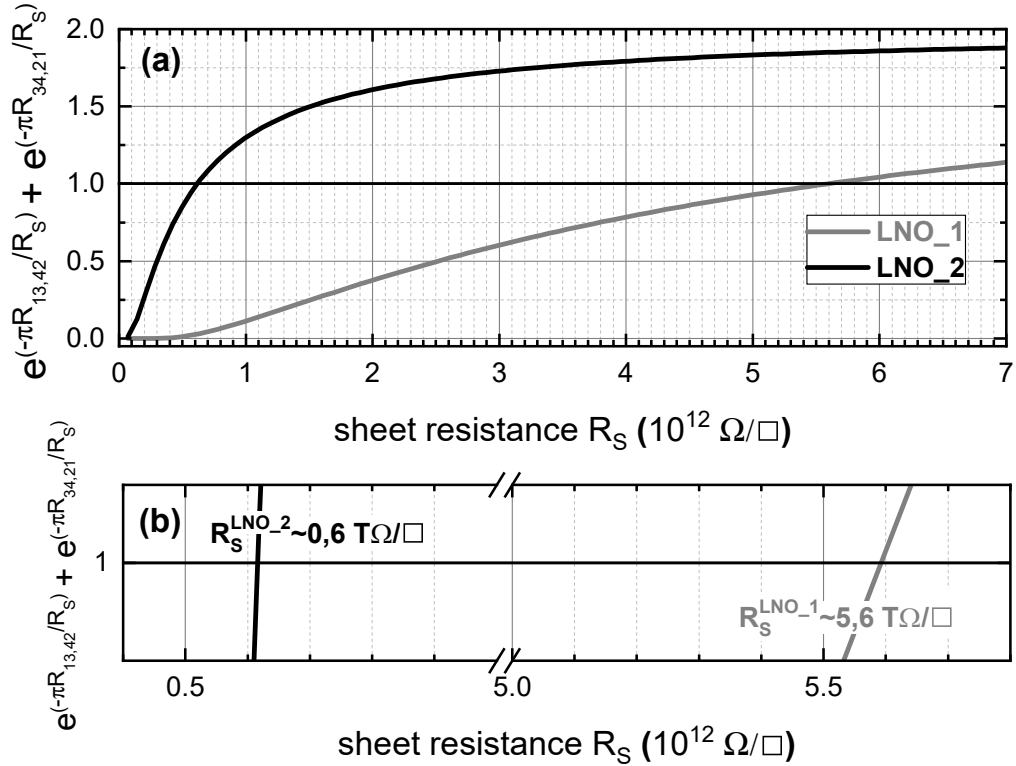


FIG. S4. Determination of the domain walls' sheet resistances R_S from a graphical solution of eq. (3) employing the measured resistance values $R_{13,42}$ and $R_{34,21}$ (cf. SI-tab. S3). Panel (b) is a close-up view of panel (a) in order to more clearly show the intersection points with the $Y=1$ -line, hence numerically revealing the R_S values.

B. Selected additional Hall-effect data

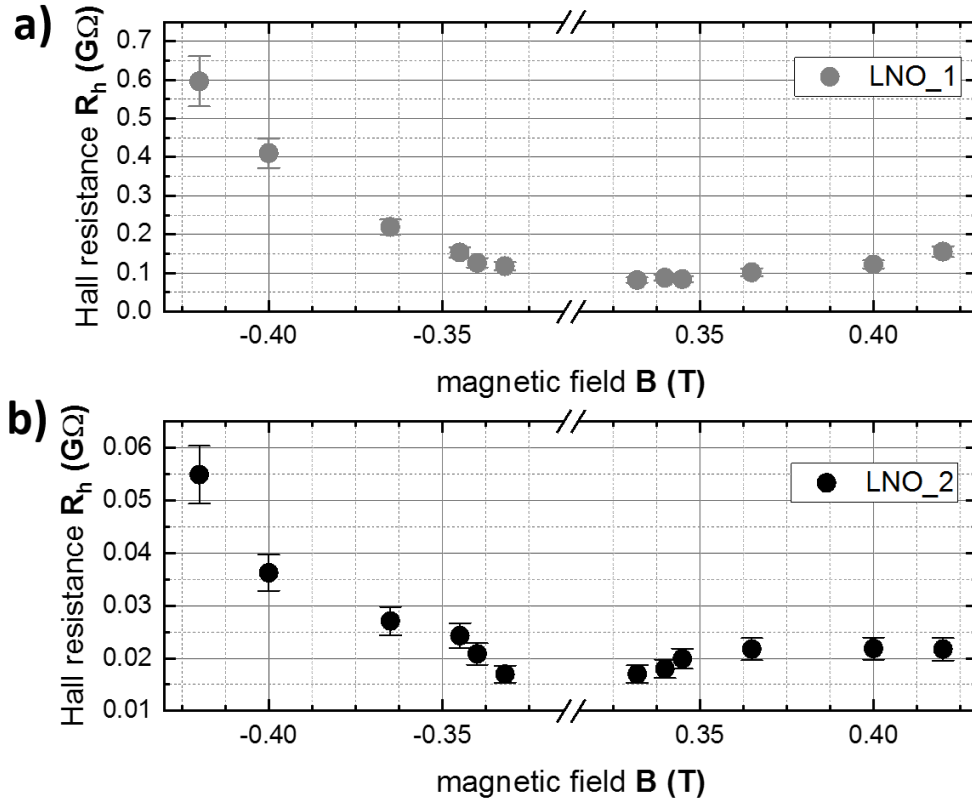


FIG. S5. B -field-direction-dependent Hall resistance for the cases of sample (a) LNO₁ and (b) LNO₂, which represent the "raw" data underlying Fig. 2 in the main text.

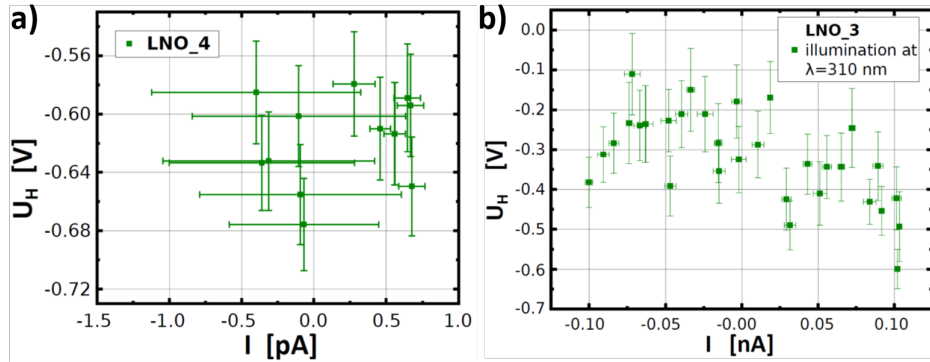


FIG. S6. Reference data showing the Hall-voltage versus current characteristics of the two **LNO bulk monodomain crystals** LNO₃ and LNO₄, that contain no domain walls at all. The same 4-electrode configuration as for samples LNO₁ and LNO₂ was applied. Then all Hall measurements were carried out in exactly the same way, i.e. (a) in the dark under an exemplary B -field of 250 mT, and (b) under the 310-nm illumination in a B -field of 110 mT. Figs. (a,b) indicate no functional relation to any of the parameters (including also no bulk photo-Hall effect), and thus determine the noise level for the two experiments.

C. Supporting microscopic domain-wall images

Complementary to the standard IV characterization, the domains were visualized by default via polarization microscopy [2D top view for both DWs, SI-figs. S7(a) and (b)]. In order to illustrate the electrode geometry, a polarization microscopy image with both, a hexagonal LNO domain and the two top electrodes, is depicted in SI-Fig. S7(c).

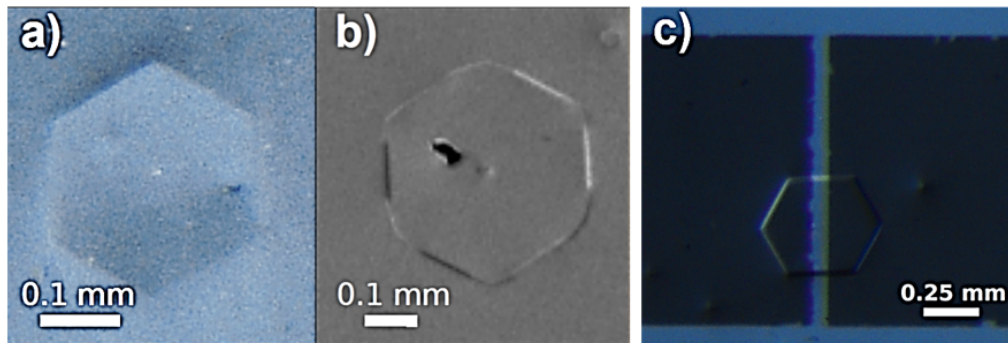


FIG. S7. Polarization microscopy images of samples (a) LNO₁ and (b) LNO₂. (c) Polarization microscopy image (top view) of a hexagonal LNO domain also showing the two top vdP chromium electrodes (black rectangles).

D. Random-Resistor-Network simulations

Normally, in 4-point Hall measurements only a single conductive sheet is measured. However, due to the specific geometry of the hexagonal domains the samples of LNO₁ and LNO₂ contain two conductive sheets in a parallel configuration, which both contribute to the Hall voltage. As discussed in the main text, this can lead to overestimations of the actual carrier densities (and conversely underestimations of the mobilities), because current flows in both sheets as shown in Fig. S8. The actual influence depends on the relation of conductivity of the two parallel sheets. In this regard, two extreme cases can be distinguished: (1) Both sheets are of equal conductivity. Hence, the applied current splits equally between both sheets leading to an overestimation of the charge carrier density and an underestimation of mobility. Hence, the extracted carrier densities need to be multiplied by a value of 0.5. Subsequently, if the mobilities are calculated in the uncorrected case, they will be overestimated by a factor of 2, respectively. (2) In contrast, one sheet might be much more conductive compared to the other one. Then, the more conductive sheet will dominate the transport measurement. Therefore, only this current will contribute to the measured Hall-voltage. In that case, no correction is necessary, i.e. the correction factor is 1 for both, as this represents the standard 4-point Hall configuration. Any real structure of two parallel sheets will require a correction between these two extremes. In our experiment, we could not measure the conductivity independently. However, we can reconstruct the (local) conductivity of each sheet based on the 3D-SHG data and a previously developed and verified random-resistor-network (RRN) model [27]. It is well established that the DW conductivity is proportional to the local DW inclination with respect to the polar axis. This can be measured with a resolution down to the μm in three dimensions with SHG microscopy [3]. The resulting scans are shown in Fig. 1 in the main text, where the local inclination is color coded. For the two contributing sheets, the local inclination is converted into a map of ohmic resistors, which are each connected to four neighbors and the value of each resistor is proportional to the sine of the local inclination. The workflow is shown for one sheet in Fig. S8.

The resulting resistor network of each sheet allows to calculate the local potential by numerically solving the Poisson equation. From the resulting potential distribution the current flowing in each node of the network is determined. Thus allowing the calculation of the ratio of current flowing through each sheet. More details on the algorithm can be found in the original work by Wolba et al. [27]. Since the charge carrier density is directly proportional to the amount of current flowing through the Hall sample, these ratios serve as correction factors for the measured charge carrier densities as well. Subsequently the comparison between measured current and the "real", i.e., simulated, current leads to a correction factor of 0.51 for LNO₁ and 0.65 for LNO₂, respectively, which are close to the ideal factor of 0.5 for two equally conductive sheets in a parallel configuration. The difference in the correction factors also mirrors the observed differences in local inclination angles and shows that LNO₂ is closer to a single sheet Hall-sample due to its inhomogeneously distributed inclination angles being more prevalent on one side than the other.

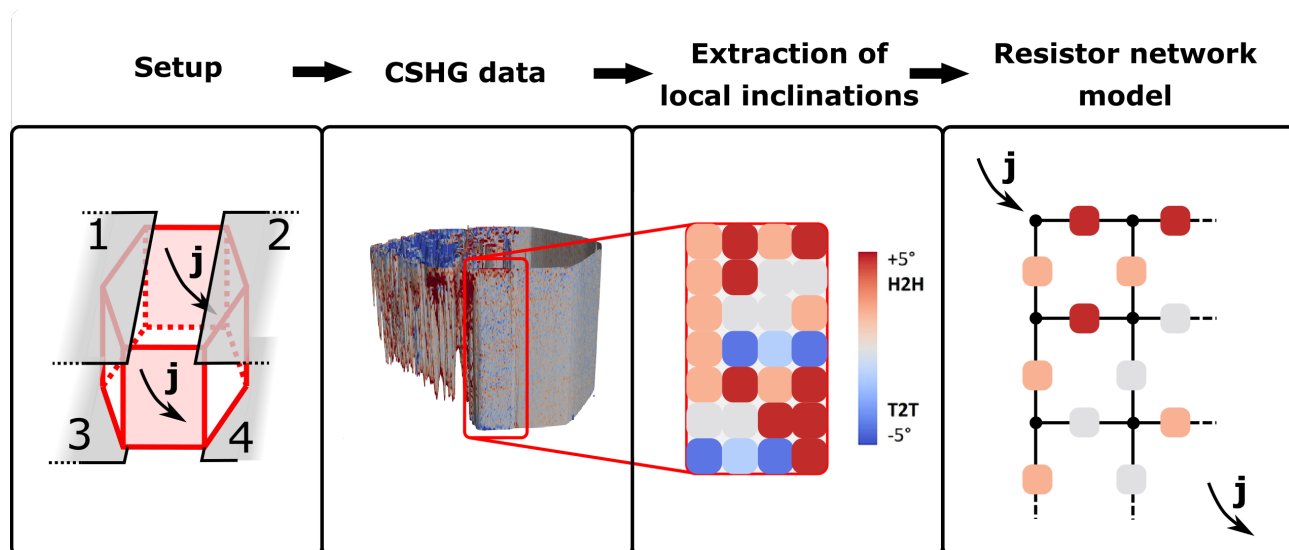


FIG. S8. Flowchart sketching the extraction of correction factors for both charge carrier density and Hall mobility, which becomes necessary due to the real structure of LNO DWs, which are not single sheets. Using second-harmonic-generation microscopy to determine the DWs local inclination angle. The inclination angles are mapped along two 2D planes and then used as the resistors in the resistor network.